IJMMM International Journal of Minerals, Metallurgy and Materials 矿物冶金与材料学报（英文版）

Enhanced detection of ppb-level NO_2 by uniform Pt-doped $ZnSnO_3$ nanocubes

Yaoyu Yin, Yanbai Shen, Sikai Zhao, Ang Li, Rui Lu, Cong Han, Baoyu Cui, and Dezhou Wei

Cite this article as:
Yaoyu Yin, Yanbai Shen, Sikai Zhao, Ang Li, Rui Lu, Cong Han, Baoyu Cui, and Dezhou Wei, Enhanced detection of ppb-level NO_2 by uniform Pt-doped $ZnSnO_3$ nanocubes, *Int. J. Miner. Metall. Mater.*, 29(2022), No. 6, pp. 1295-1303. https://doi.org/10.1007/s12613-020-2215-9

View the article online at SpringerLink or IJMMM Webpage.

International Journal of Minerals, Metallurgy and Materials
Volume 29, Number 6, June 2022, Page 1295
https://doi.org/10.1007/s12613-020-2215-9

Enhanced detection of ppb-level NO_2 by uniform Pt-doped $ZnSnO_3$ nanocubes

Yaoyu Yin[1)], *Yanbai Shen*[1,2),✉], *Sikai Zhao*[1),✉], *Ang Li*[1)], *Rui Lu*[1)], *Cong Han*[1)], *Baoyu Cui*[1)], *and Dezhou Wei*[1)]

1) School of Resources and Civil Engineering, Northeastern University, Shenyang 110819, China
2) State Key Laboratory of Rolling and Automation, Northeastern University, Shenyang 110189, China
(Received: 7 August 2020; revised: 19 October 2020; accepted: 20 October 2020)

Abstract: $ZnSnO_3$ nanocubes (ZSNCs) with various Pt concentrations (i.e., 1at%, 2at%, and 5at%) were synthesized by a simple one-pot hydrothermal method. The microstructures of pure and Pt-doped ZSNCs were characterized by X-ray diffractometry, scanning electron microscopy, transmission electron microscopy, energy-dispersive X-ray spectroscopy, and X-ray photoelectron spectroscopy. Results showed that the pure ZSNCs have a perovskite structure with a side length of approximately 600 nm; this length was reduced to 400 nm after Pt doping. Following doping, PtO_x (PtO and PtO_2) nanoparticles with a diameter of approximately 5 nm were uniformly coated on the surface of the ZSNCs. Systematic investigation of the gas-sensing abilities of the nanocubes showed that the Pt-doped ZSNCs have excellent sensing properties toward nitrogen dioxide (NO_2) gas in the operating temperature range of 75–175°C. Among the sensors prepared, that based on 1at% Pt-doped ZSNCs exhibited the best response of 16.0 toward 500 ppb NO_2 at 125°C; this response is over 11 times higher compared with that of pure ZSNCs. The enhanced NO_2 sensing mechanism of the Pt-doped ZSNCs may be attributed to the synergistic effects of catalytic activity and chemical sensitization by Pt doping.

Keywords: $ZnSnO_3$ nanocubes; Pt doping; nitrogen dioxide; gas sensor

1. Introduction

As a common polluting gas, nitrogen dioxide (NO_2), which is usually generated from industrial processes and thermal power plants, causes photochemical smog and acid rain [1]. This hazardous and toxic gas is also known to cause lung disease and respiratory infections [2–3]. According to the Health and Safety Guidelines, the limit for human exposure to 3 ppm NO_2 is less than or equal to 8 h [4]. Therefore, developing a reliable sensor with sensitive responses and low energy consumption to detect sub-ppm-level NO_2 is a crucial undertaking.

Several types of gas sensors based on different working principles have been developed for NO_2 detection, including electrochemical [5], optical [6], and resistive gas sensors [7]. Metal oxide semiconductors (MOS) are commonly used as sensing materials to detect harmful gases in the environment on account of their low cost, convenient operation, outstanding selectivity, and good reproducibility [8–9]. The sensing principle of MOS-based sensors involves resistance variations due to interactions between a pollutant gas and the surface of the sensing material. Taking n-type semiconductors as an example, different gases capture (release) electrons from (to) the conduction band to modulate the electron concentration of the sensing material and, in turn, the resistance of the sensor when it is placed in a gas environment [10]. The reaction between the gas molecules and the sensing material significantly influences the sensitivity and selectivity of the sensor. Therefore, many researchers have sought to promote the sensing reaction through various routes to fabricate high-performance gas sensors.

Various binary MOS materials, such as SnO_2 [11], ZnO [12], WO_3 [13], and In_2O_3 [14], have been widely applied over the last few decades for harmful gas detection given their unique physicochemical properties. Recent studies have focused on the fabrication of perovskite oxide sensing materials for the detection of harmful and toxic gases to promote the development of high-performance gas sensors [15–17]. $ZnSnO_3$, a typical perovskite oxide, has gradually drawn increased attention for this purpose. Zhang *et al.* [18] prepared $ZnSnO_3$ microspheres via a facile microwave-assisted process and investigated the ethanol-sensing characteristics of the resulting sensor. The authors' results demonstrated that the sensor has a high response of 47 to 50 ppm ethanol at 230°C. Zhou *et al.* [19] fabricated a high-performance ethanol gas sensor by using hollow $ZnSnO_3$ cubes as sensing materials and found that the response of the sensor to 100 ppm ethanol is 34.1 at 260°C. Chen *et al.* [20] prepared hollow $ZnSnO_3$ polyhedra via a facile hydrothermal method and obtained a maximum response value of 12.48 toward 50 ppm acetone at an optimal operating temperature of 240°C. Despite these advancements, however, current studies on Zn-

✉ Corresponding authors: Yanbai Shen E-mail: shenyanbai@mail.neu.edu.cn; Sikai Zhao E-mail: zhaosikai@mail.neu.edu.cn

SnO_3-based gas sensors generally focus on ppm-level toxic gas detection. In addition, the optimal operating temperature of the available sensors usually exceeds 200°C, thus resulting in high energy consumption and reduced reliability. To the best of our knowledge, reports on the use of $ZnSnO_3$ to detect ppb-level gases at a low operating temperature are scarce.

Noble metals (e.g., Pd, Ag, Pt, and Au) are known to enhance the gas-sensing properties of sensing materials because they not only improve the electron concentration but also promote the reaction of gas molecules with chemisorbed oxygen ions on the material surface. Chen *et al.* [21] modified ZnO nanowire surfaces with Pd by a hydrothermal method and noted significant improvements in the gas-sensing properties of the resulting material toward NO_2. Shen *et al.* [22] loaded Ag nanoparticles onto ZnO microspheres via a facile precipitation method and obtained products showing approximately 15-fold higher responses compared with pure ZnO during triethylamine gas detection. Zhang *et al.* [23] prepared Pt-decorated Fe_2O_3 nanocubes by a simple hydrothermal method and found that the resulting nanocubes exhibit 8-fold greater responses compared with pure Fe_2O_3 toward acetone. Shen *et al.* [24] discussed the effects of the noble-metal doping mode on the sensing properties of WO_3 materials and found that Au-doping could increase the sensitivity of WO_3 microspheres to NO_2 gas and reduce the optimal operating temperature. Although several studies to improve the gas-sensing properties of MOS via loading with noble-metal elements have been reported, further enhancement of the oxidizing gas-sensing performance of gas sensors based on ternary MOS materials, such as $ZnSnO_3$, by functionalization with noble metals remains a challenging endeavor.

In this work, high-performance NO_2 gas sensors based on pure and Pt-doped $ZnSnO_3$ nanocubes (ZSNCs) were fabricated via a simple one-pot hydrothermal process. The microstructure and gas-sensing properties of the resultant ZSNCs, including their morphology, crystallinity, sensor response, response/recovery speed, and selectivity to NO_2, were then systematically investigated. Finally, the gas sensing mechanism of the sensors was discussed.

2. Experimental

2.1. Chemicals

The samples were synthesized from analytically pure tin tetrachloride ($SnCl_4·5H_2O$), zinc sulfate heptahydrate ($ZnSO_4·7H_2O$), hexamethylenetetramine ($(CH_2)_6N_4$, HMT), chloroplatinic acid (H_2PtCl_6), and sodium hydroxide (NaOH). All chemicals were procured from Sinopharm Chemical Reagent Co., Ltd. Deionized water was used in all synthesis and fabrication processes.

2.2. Sample synthesis

Pure ZSNCs were prepared via a typical hydrothermal process. In the experiment, 3 mmol of $SnCl_4$, 3 mmol of $ZnSO_4$, 0.15 mmol of HMT, and 50 mL of deionized water were added into a beaker and magnetically stirred to form a milky solution. The pH value of the solution was adjusted to 11 by the dropwise addition of 1 mol/L NaOH under magnetic stirring for 1 h. Then, the mixture was maintained at 140°C for 8 h in a 200 mL hydrothermal autoclave. The resulting products were collected, cleaned with ethanol and deionized water to eliminate residual ions, and then dried at 60°C for 8 h.

Pt-doped ZSNCs were synthesized as follows. A certain amount of H_2PtCl_6 solution based on different molar ratios (i.e., 1at%, 2at%, and 5at%) of Pt to $ZnSn(OH)_6$ was added dropwise into the milky solution that prepared using a same protocol as shown in the procedure of the pure ZSNCs preparation. The pH value of the mixed solutions was adjusted to 11 by addition of 1 mol/L NaOH solution with magnetic stirring for 30 min. The obtained suspensions were transferred to a 200 mL hydrothermal autoclave and heated at 140°C for 8 h. Finally, the products were washed with deionized water and ethanol and dried in an electrical oven. The pure and Pt-doped ZSNCs were annealed at 400°C for 4 h to remove bound water and stabilize their structures and sensing properties. After annealing, the chemical formula of the products changed from $ZnSn(OH)_6$ to $ZnSnO_3$. In this work, the pure ZSNC sample was named S0 and the Pt-doped ZSNC samples with Pt concentrations of 1at%, 2at%, and 5at% were named S1, S2, and S5, respectively.

2.3. Sample characterization

The phases and crystallographic structures of the prepared samples were determined by X-ray diffractometry (XRD, PANalytical X'Pert Pro, Cu-K_α radiation, λ = 0.15406 nm). The microstructures and morphologies of the products were studied by field emission scanning electron microscopy (FESEM, Hitachi S4800; working voltage, 2 kV). Other microstructural details and the surface elemental distributions of the samples were investigated by transmission electron microscopy (TEM, JEOL 2100; working voltage, 200 kV) and energy-dispersive X-ray spectroscopy (EDS), respectively. The elemental compositions and relevant valence states of the samples were evaluated by X-ray photoelectron spectroscopy (XPS, ESCALAB 250 Xi). Here, all peaks were calibrated against the C 1s peak at 284.8 eV as the reference.

2.4. Gas sensor fabrication

The fabrication process of gas sensors based on the developed sensing materials is described in our previous work [15]. Briefly, the obtained sample powders were placed in an agate mortar and mixed with a small amount of ethanol added dropwise into the mortar. The sample powders were softly ground to form a homogenous slurry. Subsequently, the slurry was brushed evenly on the surface of a ceramic tube with two Au electrodes to form a sensing layer. A small Ni–Cr alloy wire was installed in the ceramic tube as the heater to enable the adjustment of the operating temperature of the gas sensors via voltage control. Finally, the gas sensors were dried for 1 h at room temperature and maintained at 300°C for 48 h to improve their stability prior to testing.

The gas-sensing abilities of the pure and Pt-doped ZSNCs were investigated in a static gas-sensing analytical system

(WS-30A, Weisheng Electronics Co., Ltd.). The gas sensors were operated at varying temperatures from 75 to 175°C by changing the heating voltage. Introduction of NO_2 into the test system caused immediate changes in the sensor resistance. When the sensor resistance reached a stable value, the NO_2 gas was exhausted from the test system so that the sensor resistance returned to its original value. The NO_2 concentration in the 18 L test chamber was changed from 50 to 800 ppb by mixing a certain volume of NO_2 and air using a fan. The sensor responses for the oxidizing and reducing gases were calculated as R_g/R_a and R_a/R_g, respectively, where R_g and R_a are the resistance values of the gas sensors in the target gas and atmospheric air, respectively. The response and recovery times of the sensor refer to the times required to reach a resistance alteration of 90% as the detected gas was introduced and exhausted, respectively.

3. Result and discussion

3.1. Characterizations

Fig. 1(a) shows the XRD patterns of the as-prepared products before annealing. The diffraction peaks of all four samples match those of typical fcc $ZnSn(OH)_6$ (JCPDS File No. 74-1825) well. The obtained peaks are strong and narrow, and no impurity peaks appear, thus illustrating the high purity and good crystallinity of the products. After annealing in air, $ZnSn(OH)_6$ is dehydrated into $ZnSnO_3$. Fig. 1(b) shows the corresponding XRD patterns of the annealed pure and Pt-doped ZSNCs. No sharp or high-intensity diffraction peaks are observed, which means the products are structurally transformed into amorphous materials. Dehydration of the $ZnSn(OH)_6$ precursor and increases in the disorder of the internal lattice arrangement result in the occurrence of a large number of dangling bonds, which could positively influence the gas-sensing performance of the prepared materials. No diffraction peak indicating the presence of Pt elements is observed in any of the XRD patterns collected; this result reveals the low concentration of Pt in the doped samples. However, compared with those of pure $ZnSnO_3$, the diffraction peaks of Pt-doped $ZnSnO_3$ are weaker and shift by approximately 0.1°–0.2° toward smaller 2θ values, thus confirming the incorporation of Pt into the $ZnSnO_3$ lattice.

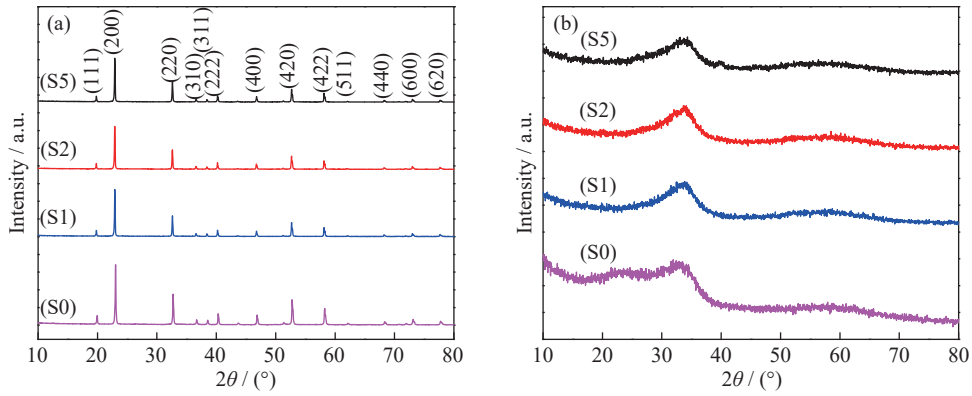

Fig. 1. XRD patterns of (a) the Pt–$ZnSn(OH)_6$ precursors and (b) annealed Pt–$ZnSnO_3$.

The morphology and microstructure of the pure and Pt-doped ZSNCs are characterized by FESEM, and the corresponding results are illustrated in Fig. 2. Fig. 2(a) reveals that the pure ZSNCs products are uniform and well-dispersed nanocubes with a side length of 600 nm. Fig. 2(b–d) shows that the cubic shape of the ZSNCs is maintained but their size is reduced to 400 nm following the introduction of Pt. Combining these findings with the above XRD results, we suggest that addition of H_2PtCl_6 to the Zn + Sn solution causes the $PtCl_6^{2-}$ ions to compete with the growth units of $Zn(OH)_4^{2-}$ and Sn^{4+} for absorption on the surface of the initial $ZnSn(OH)_6$ crystals, thus inhibiting the growth of $ZnSn(OH)_6$. Many Pt nanoparticles can be observed on the surface of ZSNCs. Moreover, at high Pt concentrations, some Pt nanoparticles aggregate together.

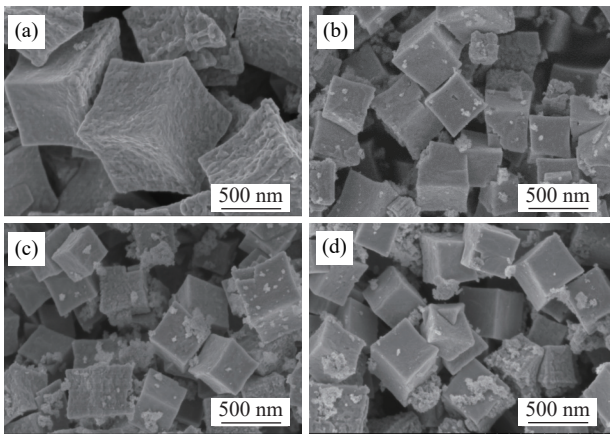

Fig. 2. FESEM images of (a) $ZnSnO_3$, (b) 1at%Pt–$ZnSnO_3$, (c) 2at%Pt–$ZnSnO_3$, and (d) 5at%Pt–$ZnSnO_3$.

The detailed structural characteristics and elemental distributions of $ZnSnO_3$ in S1 are investigated by TEM and HRTEM. The TEM images in Fig. 3(a–b) and the HRTEM image of an individual cube in Fig. 3(c) reveal the presence of several nanoparticles with a diameter of 5 nm on the surface of the ZSNCs. The measured lattice interplanar distances in Fig. 3(c), at 0.319 and 0.218 nm, match the respective measurements of the crystal planes of PtO_2 (110) and PtO (110) well. This finding demonstrates that PtO_x nanoparticles are decorated on the surface of the ZSNCs. The selected area electron diffraction (SAED) image in Fig. 3(d) reveals the

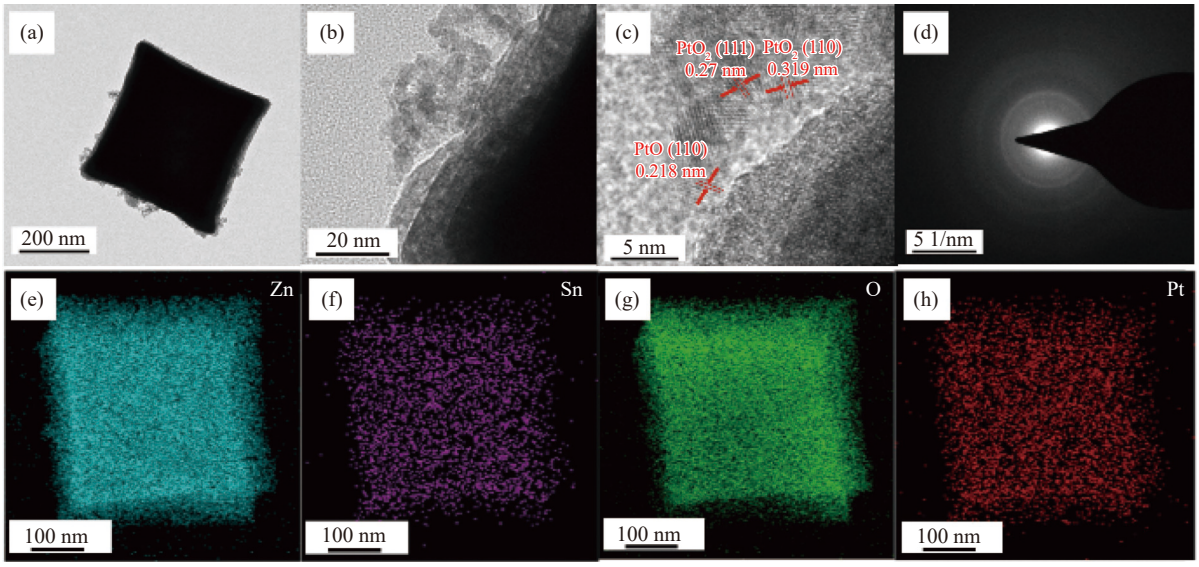

Fig. 3. (a, b) TEM, (c) HRTEM, and (d) SAED images of 1at%Pt–$ZnSnO_3$. (e–h) EDS elemental mapping images of 1at%Pt–$ZnSnO_3$.

amorphous nature of the Pt-doped ZSNCs, which agrees well with the XRD results. As seen in Fig. 3(e–h), Zn, Sn, O, and Pt are uniformly distributed on the samples, thus further confirming the presence of Pt in the final materials.

The elemental compositions and chemical valence states of S1 are characterized by XPS. As presented in Fig. 4(a), the Zn 2p spectrum can be deconvoluted into two peaks of Zn $2p_{1/2}$ (1021.8 eV) and Zn $2p_{3/2}$ (1044.8 eV), thus suggesting that Zn exists in the ZSNCs with a +2 valence state. Fig. 4(b) shows that the two strong peaks located at 486.9 and 495.4 eV coincide with Sn $3d_{5/2}$ and Sn $3d_{3/2}$, respectively, thus indicating that Sn has a +4 valence state. The high-resolution spectra of O 1s in Fig. 4(c) exhibits three peaks at 530.7, 532.3, and 533.2 eV, which could respectively be ascribed to the lattice oxygen, oxygen vacancies, and surface oxygen species of the ZSNCs. Fig. 4(d) reveals that several peaks could be obtained by dividing the raw data, which indicates that Pt exists in the ZSNCs at various chemical states. The three binding energies of 73.1, 75.8, and 78.8 eV could be attributed to Pt^{2+} $4f_{7/2}$, Pt^{4+} $4f_{5/2}$, and Pt^{4+} $4f_{7/2}$, respectively [25]. Thus, oxidized PtO_x components can be found on the surface of the ZSNCs. These findings agree with the FESEM, TEM,

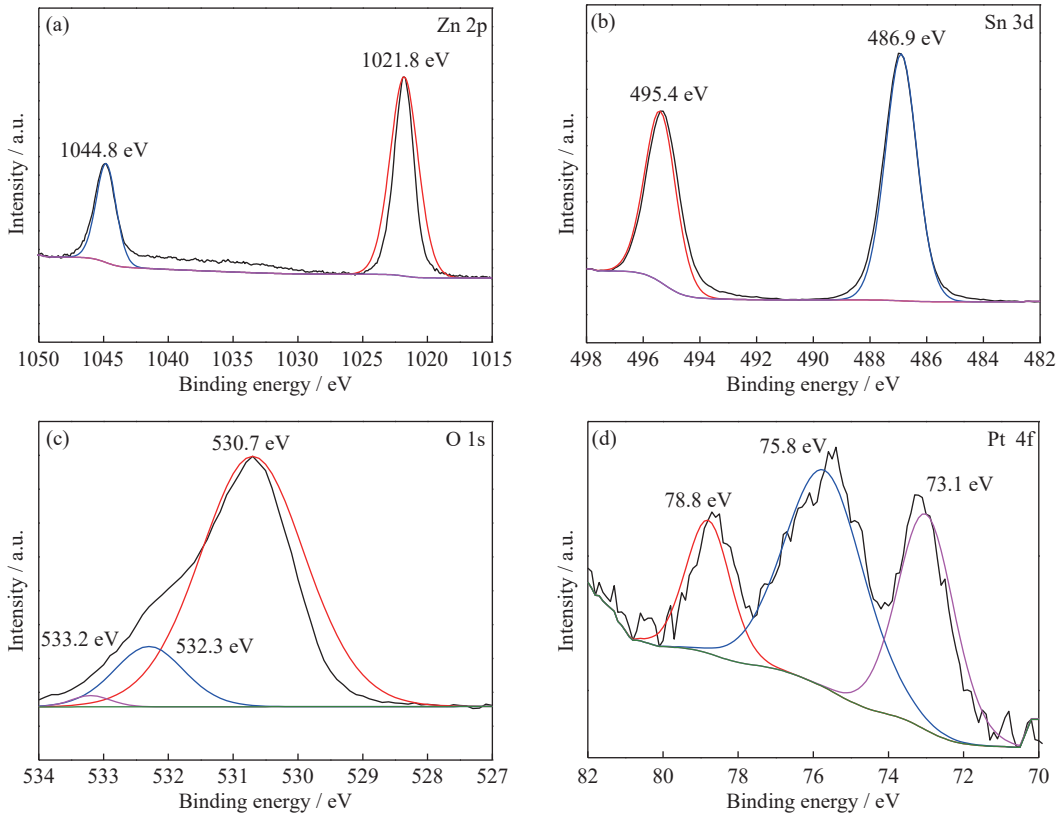

Fig. 4. XPS spectra of 1at%Pt–$ZnSnO_3$: (a) Zn region, (b) Sn region, (c) O region, and (d) Pt region.

and EDS results. The presence of Pt on the ZSNCs provides a supply of free electrons and active sites and reduces the activation energy of the gas reaction, both of which can improve the gas-sensing properties of the prepared materials [26].

3.2. Gas-sensing performance

Fig. 5(a) illustrates the response–recovery curves of the four sensors toward 500 ppb NO_2 at 125°C. All of the sensing materials show n-type semiconducting property. The sensor resistances increase to a stable value and then return to their baseline value following the injection and exhaustion of NO_2, thereby indicating good reversibility. Compared with the pure ZSNCs, the Pt-doped ZSNCs exhibit greater resistance changes, thus demonstrating their enhanced gas-sensing ability. Fig. 5(b) shows the sensors' responses to 500 ppb NO_2 as a function of the operating temperature. As the operating temperature increases, the responses of all sensors gradually increase and then decrease dramatically. The peak sensor response occurs at 125°C. Adsorption–desorption reaction equilibrium is established between the target gas molecules and the surface of the ZSNCs during gas sensing. On the one hand, according to the Gibbs function, the chemical reaction occurs more thoroughly as the reaction temperature increases, which means the chemisorbed NO_2 can obtain more electrons from the ZSNCs. Thus, increasing the operating temperature can improve the sensing properties of the prepared materials. On the other hand, gas adsorption onto solids is an exothermic process. According to the van't Hoff equation, the desorption speed is faster than the adsorption speed at higher operating temperatures. Therefore, the maximum sensor response could be obtained at the optimal operating temperature. The responses of the Pt-doped ZSNCs are higher than those of the pure ZSNCs in the operating temperature range of 75–175°C. The responses of different sensors toward 500 ppb NO_2 at 125°C are presented in Fig. 5(c). The sensor based on pure ZSNCs has a response of 1.5, which is much lower than those of the sensors based on Pt-doped ZSNCs. Indeed, the response of the S1-based sensor toward 500 ppb NO_2 is 16.0, which is over 11 times higher than that of the pure ZSNC-based sensor. Interestingly, as the Pt concentration increases, the responses of the sensors gradually decrease, likely because the increased presence of Pt nanoparticles destroys the crystal structure and reduces the active sites of the ZSNCs. Despite this limitation, the S3-based sensor shows better responses toward NO_2 than the pure ZSNCs, which suggests that Pt can promote the reaction between NO_2 and the sensing material.

High response/recovery rates are a must for gas sensors used in harmful gas detection applications. Fig. 6 shows the response and recovery time of all sensors toward 500 ppb NO_2 at 125°C. Among the sensors studied, the S0-based sensor has the lowest response and recovery times because of its poor response to NO_2. As seen in Fig. 6, the response/recovery times of the sensors shows significant declines at different operating temperatures mainly because higher operating temperatures result in more rapid gas diffusion rates and, in turn, faster adsorption and desorption of NO_2. The sensors

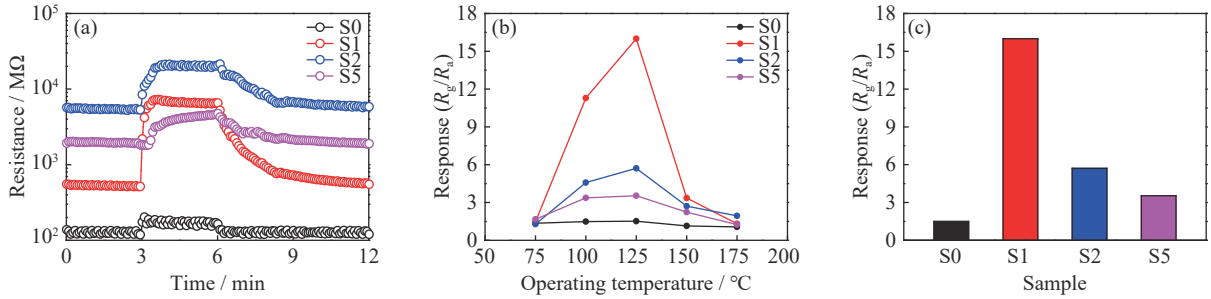

Fig. 5. (a) Response and recovery curves of the sensors to 500 ppb NO_2 at 125°C. (b) Responses of the sensors to 500 ppb NO_2 at different operating temperatures. (c) Responses of the sensors to 500 ppb NO_2 at 125°C.

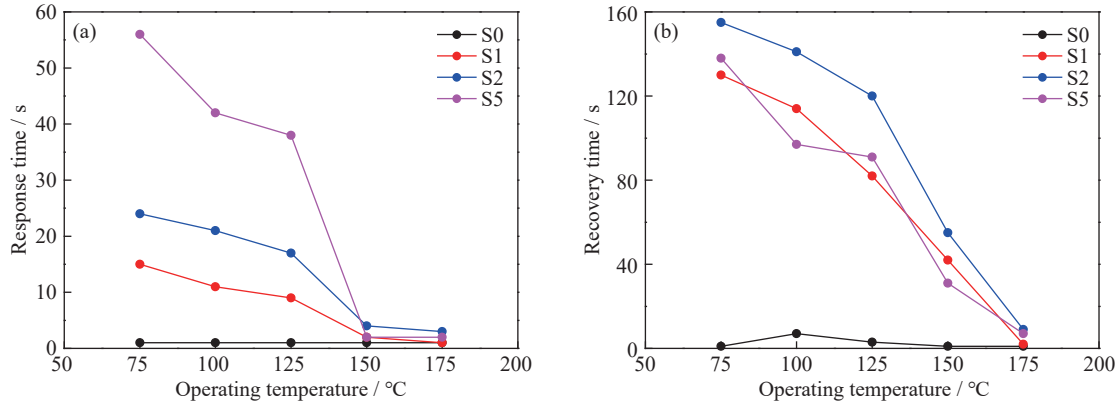

Fig. 6. (a) Response and (b) recovery times of the as-fabricated sensors after exposure to 500 ppb NO_2 as a function of the operating temperature.

based on S1, S2, and S5 respectively show response times of 9, 17, and 38 s toward 500 ppb NO_2 and recovery times of 82, 120, and 91 s at 125°C. These results demonstrate that a moderate level of Pt doping onto the ZSNCs can greatly enhance the response value and response/recovery rates of the latter.

Fig. 7(a) shows the dynamic response and recovery curves of the sensors toward 50–800 ppb NO_2 at the optimal operating temperature of 125°C. The resistance values of all sensors increase when NO_2 is introduced to the test chamber and then return to their original values when NO_2 is exhausted from the chamber. As the NO_2 concentration increases, the resistance change of all sensors increases. The resistance changes of the sensors show the order of S0 < S5 < S2 < S1. Moreover, all sensors exhibit good reversibility during the complete sensing test. Fig. 7(b) illustrates the sensor responses as a function of NO_2 concentration. A good linear relationship between the sensor response and NO_2 concentrations of 50–800 ppb could be observed. The responses of the S0-based sensor upon exposure to 50, 100, 200, 500, and 800 ppb NO_2 are 1.01, 1.10, 1.22, 1.51, and 1.89, respectively. By comparison, the responses of the Pt-doped ZSNCs are several times greater than those of the pure ZSNCs. In particular, the responses of the S1-based sensor to 50, 100, 200, 500, and 800 ppb NO_2 are 1.31, 3.76, 7.30, 16.0, and 23.28, respectively.

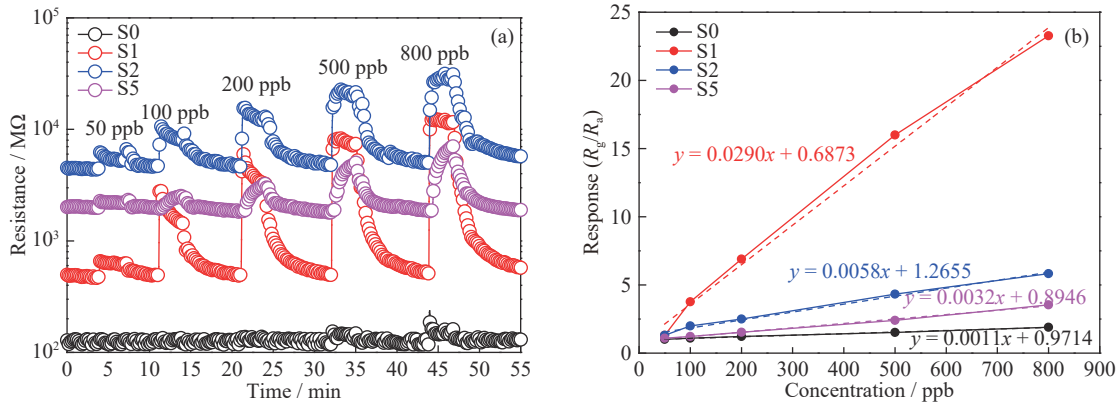

Fig. 7. (a) Dynamic response–recovery curves of the as-fabricated sensors following exposure to different concentrations of NO_2 at 125°C. (b) Relationships between the sensor response and NO_2 concentration.

Power functions are usually used to represent the relationship between the sensor response and gas concentration.

$$y = KP^{\alpha} \quad (1)$$

where y and P are the sensor response and gas concentration, respectively, K is a constant, and α is an exponent. Table 1 summarizes the specific formulas of the fitting curves of the sensors. All of the equations are linear because $\alpha = 1$. Furthermore, the correlation coefficients (R^2) of the fitting curves for all sensors exceed 0.99, thus indicating the excellent linear relationship between the sensor response and NO_2 concentrations in the range of 100–800 ppb. The value of α mainly depends on the oxygen species adsorbed on the ZSNCs, which leads to different reactions with the target gas. The values of α when O_2^- and O^- are chemisorbed on the ZSNCs are 0.5 and 1, respectively. If the value of α is between 0.5 and 1, the chemisorbed oxygen is composed of these two types of oxygen species. Therefore, the composition of the adsorbed oxygen could be calculated from the value of α.

Reproducibility and stability are key indices for gas sensors in industrial production and practical applications.

Table 1. Specific formulas of the fitting curves of all sensors

Sample No.	Equation	R^2
S0	$y = 0.0011x + 0.9714$	0.995
S1	$y = 0.0290x + 0.6873$	0.994
S2	$y = 0.0058x + 1.2655$	0.992
S5	$y = 0.0032x + 0.8946$	0.997

Fig. 8 illustrates the response curves of each sensor exposed to 500 ppb NO_2 at 125°C over three complete air–NO_2–air cycles. All of the sensors show good response and recovery properties. Following NO_2 introduction or exhaustion, the resistance of the sensors change in an identical manner during the sensing test under the same NO_2 concentration. These results demonstrate that sensors based on the as-prepared sensing materials have excellent reproducibility and reversibility.

High selectivity is a crucial property for sensing materials. The responses of the sensors toward various gases with concentrations much higher than 500 ppb are investigated. Fig. 9

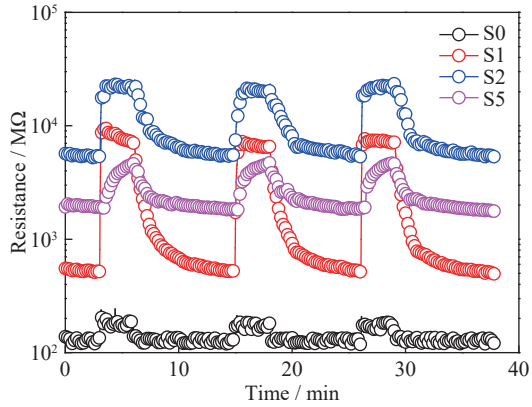

Fig. 8. Resistance changes of the as-fabricated sensors over three cycles of exposure to 500 ppb NO_2 at 125°C.

shows that the S0-based sensor exhibits a similar and low response, i.e., less than 1.5, to different gases. Pt doping significantly enhances the selectivity of the ZSNCs to NO_2. For example, whereas the response of the S1-based sensor to 500 ppb NO_2 is as high as 16.0, its responses to 100 ppm acetone, 100 ppm toluene, 100 ppm methanol, 1000 ppm hydrogen, and 1000 ppm methane are as low as 1.28, 1.54, 1.15, 1.28, and 1.07, respectively, thus suggesting virtually no response to these gases. The sensors obtained from S2 and S5 also show excellent selectivity to NO_2, which may be explained by the fact that NO_2 has higher adsorption energy and electron affinity to the sensor than the other gas molecules. These results confirm that Pt doping promotes the reaction between NO_2 and the sensing materials.

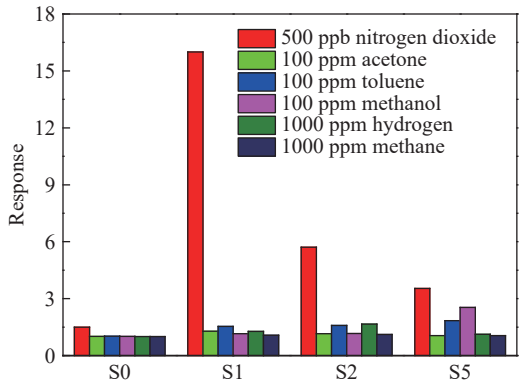

Fig. 9. Responses of the as-fabricated sensors to different types of gases at 125°C.

The gas-sensing properties of the as-prepared Pt-doped ZSNCs were compared with those of other gas sensors based on different MOS materials. Previously developed sensors present a number of shortcomings, including low responses and high operating temperatures. As observed in Table 2, compared with other sensors, the S1-based gas sensor developed in this work shows a much higher response to only 500 ppb NO_2. Moreover, the S1-based gas sensor has excellent ppb-level NO_2 gas-sensing properties at a lower operating temperature. A lower operating temperature is desirable for lower energy consumption.

3.3. Gas-sensing mechanism

The developed ZSNCs exhibit n-type semiconducting properties. The gas-sensing properties of the ZSNCs greatly depend on gas adsorption/desorption, the gas reaction, and carrier transfer on the material surface. When a sensor is placed in an air atmosphere, oxygen molecules are chemisorbed on the surface of the sensing material by trapping carriers from its conduction band. As more electrons are caught by oxygen, a depletion layer forms near the material surface [15,37]. This layer not only decreases the electron concentration but also impedes the carrier transfer of the sensing materials. Oxygen may be transformed into different species according to Eqs. (2)–(4) at various operating temperatures.

$$O_2(\text{gas}) \rightarrow O_2(\text{adsorption}) \quad (2)$$

$$O_2(\text{adsorption}) + e^- \rightarrow O_2^-(\text{adsorption}) \quad (3)$$

$$O_2^-(\text{adsorption}) + e^- \rightarrow 2O^-(\text{adsorption}) \quad (4)$$

Free electrons, which exist in thle conduction band of the sensing materials, can be captured by the adsorbed NO_2 molecules when the sensors are placed in a NO_2 atmosphere because of the stronger electron-withdrawing capacity of NO_2 compared with that of oxygen. Thus, the free electron concentration decreases, resulting in the expansion of the electron depletion layer, and the sensor resistance increases [38]. The possible reaction routes are presented in Eqs. (5)–(6).

$$NO_2 + O_2^- + 2e^- \rightarrow NO_2^- + 2O^- \quad (5)$$

$$NO_2 + e^- \rightarrow NO_2^- \quad (6)$$

The NO_2 gas-sensing properties of the pure ZSNCs are significantly enhanced by Pt doping through the synergistic effects of catalytic activities and chemical sensitization of noble elements [39]. Pt doping on the surface of the ZSNCs creates more active sites for NO_2 adsorption, and more NO_2 can capture more electrons from the conduction band. Under the spillover effect of noble metals, the detected gases are transmitted from PtO_x to the surface of the ZSNCs and dispersed uniformly, thus further increasing the resistance of the sensing materials and achieving high sensor responses. The presence of PtO_x on the ZSNCs also forms a Schottky barrier

Table 2. NO_2-sensing performance of gas sensors based on different MOS materials

Material	Temperature / °C	Concentration / ppm	Response (R_a/R_g)	Ref.
ZnO–Pt films	200	1	18.19	[27]
Ag–Fe_2O_3 core–shell	150	4	3.5	[28]
Au–CuO nanowires	300	1	2.9	[29]
Pd–ZnO nanowires	100	1	13.5	[21]
Pd–V_2O_5 nanorods	200	100	1.75	[30]
Pt–WO_3 films	150	1	11.24	[31]
Pt–In_2O_3 nanoparticles	250	5	1904	[32]
Ag–WO_3 films	200	3	12.22	[33]
TiO_2@Au nanorods	250	5	136.5	[34]
Pd–MoO_3 nanobelts	200	100	1.95	[35]
Au–ZnO nanowires	150	1	31.4	[36]
Pt–$ZnSnO_3$ nanocubes	125	0.5	16.0	This work

[40]. The PtO_x decorative layer can expand the electron depletion layer and inhibit electron transfer. Therefore, Pt-doped ZSNCs show a higher baseline resistance compared with pure ZSNCs. When NO_2 comes into contact with the sensing materials, the gas molecules capture free electrons from the ZSNCs through PtO_x, and the electron depletion layer expands, as illustrated in Fig. 10. This expansion results in a greater difference in the resistance value between different gases of air and NO_2.

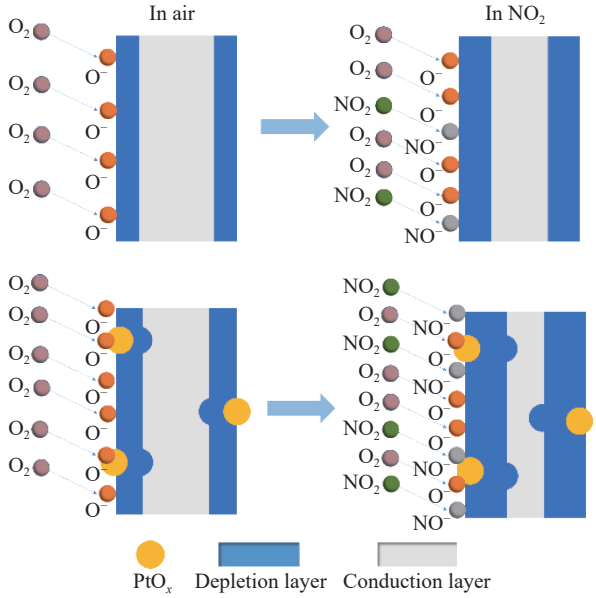

Fig. 10. Schematic diagrams of the gas-sensing mechanism of Pt–$ZnSnO_3$ for NO_2.

The size of the PtO_x nanoparticles is another essential factor influencing the sensing properties of the sensors. The sensing reaction of surface-controlled MOS sensors only takes place in the near-surface region of the materials. Many studies have proven that the sensing performance of a material can be greatly improved by decreasing the size of the material unit to less than the Debye length [41–42]. Thus, reducing the physical size of the sensing materials may be an effective route to enhance their gas-sensing performance. This study demonstrates that small highly dispersible PtO_x nanoparticles could significantly improve the response and selectivity of the prepared sensors. However, the noble-metal oxides aggregate under Pt concentrations of 2at% and 5at%, thus reducing the availability of active adsorption sites and effective surface area. Among the Pt-based sensors, that prepared from 1at% Pt-doped ZSNCs reveals the best sensing performance.

4. Conclusion

Perovskite-structured pure and Pt-doped ZSNCs were prepared by a facile hydrothermal process. Whereas pure ZSNCs showed a side length of approximately 600 nm, Pt-doped ZSNCs showed a side length of only 400 nm. PtO or PtO_2 nanoparticles were uniformly functionalized on the ZSNC surface. The NO_2-sensing performance of the prepared materials was significantly enhanced by Pt doping. The optimal operating temperature of all sensors for NO_2 sensing was as low as 125°C. In particular, the 1at%Pt-based ZSNC sensor exhibited a peak response value of 16.0 toward 500 ppb NO_2, which is much higher than the response of the pure ZSNC-based sensor (i.e., 1.5) under the same conditions. The relationship between the sensor response and NO_2 concentration complied with a linear law, and the improved sensing mechanism of the Pt-based ZSNCs was explained by the combination of enhanced catalytic activity and chemical sensitization afforded by noble-metal oxides. The results indicate that the ZSNCs developed in this work are a promising material for NO_2 detection and confirm that Pt doping can effectively enhance the sensing performance of ternary metal oxides.

Acknowledgements

This work was financially supported by the National Natural Science Foundation of China (Nos. 51674067 and 51422402), the Fundamental Research Funds for the Central Universities (Nos. N180102032, N180106002, and N180408018), the Liaoning Revitalization Talents Program (No. XLYC1807160), and the Open Foundation of State Environmental Protection Key Laboratory of Mineral Metallurgical Resources Utilization and Pollution Control (No. HB201902).

Conflict of Interest

The authors declare no potential conflict of interest.

References

[1] G.D. Li, Y.B. Shen, P.F. Zhou, F.L. Hao, P. Fang, D.Z. Wei, D. Meng, and X.G. San, Design and application of highly responsive and selective rGO–SnO_2 nanocomposites for NO_2 monitoring, *Mater. Charact.*, 163(2020), art. No. 110284.

[2] S. Jain, A. Paliwal, V. Gupta, and M. Tomar, Long Range Surface Plasmons assisted highly sensitive and room temperature operated NO_2 gas sensor, *Sens. Actuat. B Chem.*, 311(2020), art. No. 127897.

[3] Y. Ogen, Assessing nitrogen dioxide (NO_2) levels as a contributing factor to coronavirus (COVID-19) fatality, *Sci. Total. Environ.*, 726(2020), art. No. 138605.

[4] W. Liu, L. Xu, K. Sheng, C. Chen, X.Y. Zhou, B. Dong, X. Bai, S. Zhang, G.Y. Lu, and H.W. Song, APTES-functionalized thin-walled porous WO_3 nanotubes for highly selective sensing of NO_2 in a polluted environment, *J. Mater. Chem. A*, 6(2018), No. 23, p. 10976.

[5] P. Kuberský, T. Syrový, A. Hamáček, S. Nešpůrek, and L. Syrová, Towards a fully printed electrochemical NO_2 sensor on a flexible substrate using ionic liquid based polymer electrolyte, *Sens. Actuat. B Chem.*, 209(2015), p. 1084.

[6] O. Worsfold, C. Malins, M.G. Forkan, I.R. Peterson, B.D. MacCraith, and D.J. Walton, Optical NO_2 sensing based on sol–gel entrapped azobenzene dyes, *Sens. Actuat. B Chem.*, 56(1999), No. 1-2, p. 15.

[7] J. Zhao, T.L. Yang, Y.P. Liu, Z.Y. Wang, X.W. Li, Y.F. Sun, Y. Du, Y.C. Li, and G.Y. Lu, Enhancement of NO_2 gas sensing response based on ordered mesoporous Fe-doped In_2O_3, *Sens. Actuat. B Chem.*, 191(2014), p. 806.

[8] S.K. Zhao, Y.B. Shen, P.F. Zhou, J. Zhang, W. Zhang, X.X.

Chen, D.Z. Wei, P. Fang, and Y.S. Shen, Highly selective NO_2 sensor based on p-type nanocrystalline NiO thin films prepared by sol–gel dip coating, *Ceram. Int.*, 44(2018), No. 1, p. 753.
[9] J. van den Broek, S. Abegg, S.E. Pratsinis, and A.T. Güntner, Highly selective detection of methanol over ethanol by a handheld gas sensor, *Nat. Commun.*, 10(2019), art. No. 4220.
[10] J.M. Smulko, M. Trawka, C.G. Granqvist, R. Ionescu, F. Annanouch, E. Llobet, and L.B. Kish, New approaches for improving selectivity and sensitivity of resistive gas sensors: A review, *Sens. Rev.*, 35(2015), No. 4, p. 340.
[11] Y.J. Kwon, S.Y. Kang, P. Wu, Y. Peng, S.S. Kim, and H.W. Kim, Selective improvement of NO_2 gas sensing behavior in SnO_2 nanowires by ion-beam irradiation, *ACS Appl. Mater. Interfaces*, 8(2016), No. 21, p. 13646.
[12] R. Kumar, O. Al-Dossary, G. Kumar, and A. Umar, Zinc oxide nanostructures for NO_2 gas–sensor applications: A review, *Nano Micro Lett.*, 7(2015), No. 2, p. 97.
[13] J. Zeng, M. Hu, W.D. Wang, H.Q. Chen, and Y.X. Qin, NO_2-sensing properties of porous WO_3 gas sensor based on anodized sputtered tungsten thin film, *Sens. Actuat. B Chem.*, 161(2012), No. 1, p. 447.
[14] Y.B. Shen, X.X. Zhong, J. Zhang, T.T. Li, S.K. Zhao, B.Y. Cui, D.Z. Wei, Y.H. Zhang, and K.F. Wei, *In-situ* growth of mesoporous In_2O_3 nanorod arrays on a porous ceramic substrate for ppb-level NO_2 detection at room temperature, *Appl. Surf. Sci.*, 498(2019), art. No. 143873.
[15] Y.Y. Yin, Y.B. Shen, P.F. Zhou, R. Lu, A. Li, S.K. Zhao, W.G. Liu, D.Z. Wei, and K.F. Wei, Fabrication, characterization and n-propanol sensing properties of perovskite-type $ZnSnO_3$ nanospheres based gas sensor, *Appl. Surf. Sci.*, 509(2020), art. No. 145335.
[16] W. Wei, S.J. Guo, C. Chen, L. Sun, Y. Chen, W.B. Guo, and S.P. Ruan, High sensitive and fast formaldehyde gas sensor based on Ag-doped $LaFeO_3$ nanofibers, *J. Alloys Compd.*, 695(2017), p. 1122.
[17] G.H. Jain, L.A. Patil, M.S. Wagh, D.R. Patil, S.A. Patil, and D.P. Amalnerkar, Surface modified $BaTiO_3$ thick film resistors as H_2S gas sensors, *Sens. Actuat. B Chem.*, 117(2006), No. 1, p. 159.
[18] D. Zhang, Y.Q. Zhang, Y. Fan, N. Luo, Z.X. Cheng, and J.Q. Xu, Micro-spherical $ZnSnO_3$ material prepared by microwave-assisted method and its ethanol sensing properties, *Chin. Chem. Lett.*, 31(2020), No. 8, p. 2087.
[19] T.T. Zhou, T. Zhang, R. Zhang, J.N. Deng, Z. Lou, G.Y. Lu, and L.L. Wang, Highly sensitive sensing platform based on ZnSnO_3 hollow cubes for detection of ethanol, *Appl. Surf. Sci.*, 400(2017), p. 262.
[20] Q. Chen, S.Y. Ma, H.Y. Jiao, G.H. Zhang, H. Chen, X.L. Xu, H.M. Yang, and Z. Qiang, Synthesis of novel $ZnSnO_3$ hollow polyhedrons with open nanoholes: Enhanced acetone-sensing performance, *Ceram. Int.*, 43(2017), No. 1, p. 1617.
[21] X.X. Chen, Y.B. Shen, P.F. Zhou, S.K. Zhao, X.X. Zhong, T.T. Li, C. Han, D.Z. Wei, and D. Meng, NO_2 sensing properties of one-pot-synthesized ZnO nanowires with Pd functionalization, *Sens. Actuat. B Chem.*, 280(2019), p. 151.
[22] Z. Shen, X.D. Zhang, R.N. Mi, M. Liu, Y. Chen, C. Chen, and S.P. Ruan, On the high response towards TEA of gas sensors based on Ag-loaded 3D porous ZnO microspheres, *Sens. Actuat. B Chem.*, 270(2018), p. 492.
[23] S.D. Zhang, M.J. Yang, K.Y. Liang, A. Turak, B.X. Zhang, D. Meng, C.X. Wang, F.D. Qu, W.L. Cheng, and M.H. Yang, An acetone gas sensor based on nanosized Pt-loaded Fe_2O_3 nanocubes, *Sens. Actuat. B Chem.*, 290(2019), p. 59.
[24] Y.B. Shen, H.S. Bi, T.T. Li, X.X. Zhong, X.X. Chen, A.F. Fan, and D.Z. Wei, Low-temperature and highly enhanced NO_2 sensing performance of Au-functionalized WO_3 microspheres with a hierarchical nanostructure, *Appl. Surf. Sci.*, 434(2018), p. 922.
[25] B.X. Yang, J.Y. Liu, H. Qin, Q. Liu, X.Y. Jing, H.Q. Zhang, R.M. Li, G.Q. Huang, and J. Wang, PtO_2-nanoparticles functionalized CuO polyhedrons for n-butanol gas sensor application, *Ceram. Int.*, 44(2018), No. 9, p. 10426.
[26] Y.B. Shen, T. Yamazaki, Z.F. Liu, D. Meng, and T. Kikuta, Hydrogen sensors made of undoped and Pt-doped SnO_2 nanowires, *J. Alloys Compd.*, 488(2009), No. 1, p. L21.
[27] L. Giancaterini, C. Cantalini, M. Cittadini, M. Sturaro, M. Guglielmi, A. Martucci, A. Resmini, and U. Anselmi-Tamburini, Au and Pt nanoparticles effects on the optical and electrical gas sensing properties of sol–gel-based ZnO thin-film sensors, *IEEE Sens. J.*, 15(2015), No. 2, p. 1068.
[28] A. Mirzaei, K. Janghorban, B. Hashemi, M. Bonyani, S.G. Leonardi, and G. Neri, A novel gas sensor based on Ag/Fe_2O_3 core–shell nanocomposites, *Ceram. Int.*, 42(2016), No. 16, p. 18974.
[29] J.S. Lee, A. Katoch, J.H. Kim, and S.S. Kim, Effect of Au nanoparticle size on the gas-sensing performance of p-CuO nanowires, *Sens. Actuat. B Chem.*, 222(2016), p. 307.
[30] A.A. Mane, M.P. Suryawanshi, J.H. Kim, and A.V. Moholkar, Superior selectivity and enhanced response characteristics of palladium sensitized vanadium pentoxide nanorods for detection of nitrogen dioxide gas, *J. Colloid Interface Sci.*, 495(2017), p. 53.
[31] H. Liu, Y.H. Xu, X. Zhang, W.R. Zhao, A.J. Ming, and F. Wei, Enhanced NO_2 sensing properties of Pt/WO_3 films grown by glancing angle deposition, *Ceram. Int.*, 46(2020), No. 13, p. 21388.
[32] K. Inyawilert, D. Channei, N. Tamaekong, C. Liewhiran, A. Wisitsoraat, A. Tuantranont, and S. Phanichphant, Pt-doped In_2O_3 nanoparticles prepared by flame spray pyrolysis for NO_2 sensing, *J. Nanopart. Res.*, 18(2016), No. 2, p. 40.
[33] C. Kamble, M. Panse, and A. Nimbalkar, Ag decorated WO_3 sensor for the detection of sub-ppm level NO_2 concentration in air, *Mater. Sci. Semicond. Process.*, 103(2019), art. No. 104613.
[34] D.V. Ponnuvelu, B. Pullithadathil, A.K. Prasad, S. Dhara, K. Mohamed, A.K. Tyagi, and B. Raj, Highly sensitive, atmospheric pressure operatable sensor based on Au nanoclusters decorated TiO_2@Au heterojunction nanorods for trace level NO_2 gas detection, *J. Mater. Sci. Mater. Electron.*, 28(2017), No. 13, p. 9738.
[35] A.A. Mane and A.V. Moholkar, Palladium (Pd) sensitized molybdenum trioxide (MoO_3) nanobelts for nitrogen dioxide (NO_2) gas detection, *Solid State Electron.*, 139(2018), p. 21.
[36] X.X. Chen, Y.B. Shen, X.X. Zhong, T.T. Li, S.K. Zhao, P.F. Zhou, C. Han, D.Z. Wei, and Y.S. Shen, Synthesis of ZnO nanowires/Au nanoparticles hybrid by a facile one-pot method and their enhanced NO_2 sensing properties, *J. Alloys Compd.*, 783(2019), p. 503.
[37] S.K. Zhao, Y.B. Shen, P.F. Zhou, X.X. Zhong, C. Han, Q. Zhao, and D.Z. Wei, Design of Au@WO_3 core−shell structured nanospheres for ppb-level NO_2 sensing, *Sens. Actuat. B Chem.*, 282(2019), p. 917.
[38] S. Thirumalairajan, K. Girija, V.R. Mastelaro, and N. Ponpandian, Surface morphology-dependent room-temperature $LaFeO_3$ nanostructure thin films as selective NO_2 gas sensor prepared by radio frequency magnetron sputtering, *ACS Appl. Mater. Interfaces*, 6(2014), No. 16, p. 13917.
[39] L. Liao, H.X. Mai, Q. Yuan, H.B. Lu, J.C. Li, C. Liu, C.H. Yan, Z.X. Shen, and T. Yu, Single CeO_2 nanowire gas sensor supported with Pt nanocrystals: Gas sensitivity, surface bond states, and chemical mechanism, *J. Phys. Chem. C*, 112(2008), No. 24, p. 9061.
[40] S.J. Chang, W.Y. Weng, C.L. Hsu, and T.J. Hsueh, High sensitivity of a ZnO nanowire-based ammonia gas sensor with Pt nano-particles, *Nano Commun. Netw.*, 1(2010), No. 4, p. 283.
[41] N. Yamazoe, New approaches for improving semiconductor gas sensors, *Sens. Actuat. B Chem.*, 5(1991), No. 1-4, p. 7.
[42] S.K. Zhao, Y.B. Shen, P.F. Zhou, F.L. Hao, X.Y. Xu, S.L. Gao, D.Z. Wei, Y.X. Ao, and Y.S. Shen, Enhanced NO_2 sensing performance of ZnO nanowires functionalized with ultra-fine In_2O_3 nanoparticles, *Sens. Actuat. B Chem.*, 308(2020), art. No. 127729.